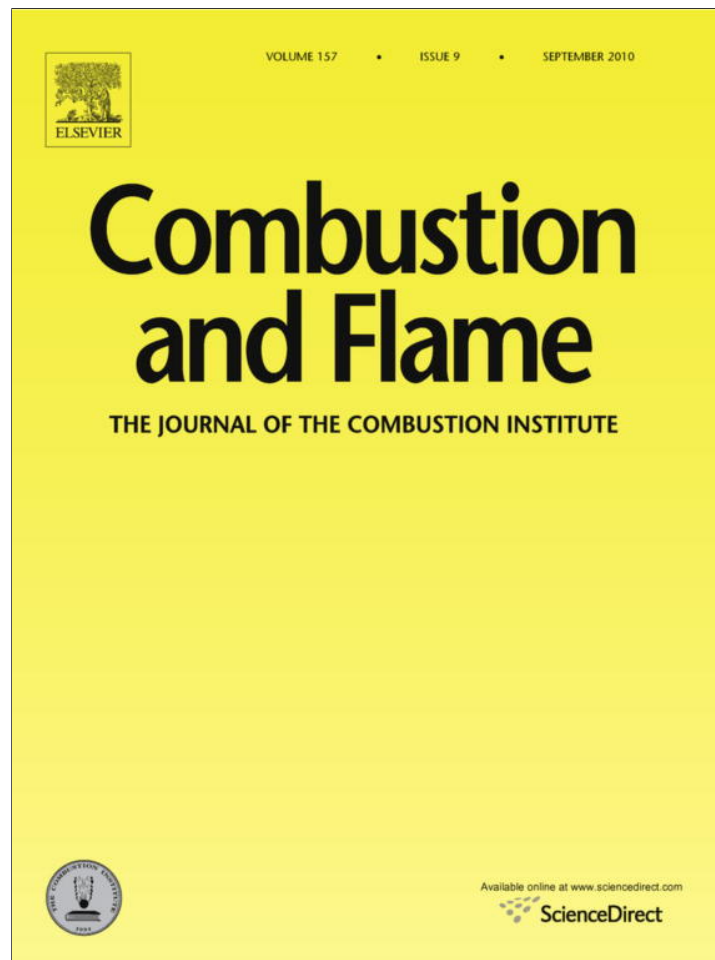


Provided for non-commercial research and education use.
Not for reproduction, distribution or commercial use.



This article appeared in a journal published by Elsevier. The attached copy is furnished to the author for internal non-commercial research and education use, including for instruction at the authors institution and sharing with colleagues.

Other uses, including reproduction and distribution, or selling or licensing copies, or posting to personal, institutional or third party websites are prohibited.

In most cases authors are permitted to post their version of the article (e.g. in Word or Tex form) to their personal website or institutional repository. Authors requiring further information regarding Elsevier's archiving and manuscript policies are encouraged to visit:

<http://www.elsevier.com/copyright>



Contents lists available at ScienceDirect

Combustion and Flame

journal homepage: www.elsevier.com/locate/combustflame

Catalytic partial oxidation of iso-octane over rhodium catalysts: An experimental, modeling, and simulation study

M. Hartmann^a, L. Maier^b, H.D. Minh^a, O. Deutschmann^{a,b,*}

^a Institute for Chemical Technology and Polymer Chemistry, Karlsruhe Institute of Technology (KIT), Kaiserstraße 12, D-76128 Karlsruhe, Germany

^b Institute for Nuclear and Energy Technology, Karlsruhe Institute of Technology (KIT), Kaiserstraße 12, D-76128 Karlsruhe, Germany

ARTICLE INFO

Article history:

Received 8 November 2009

Received in revised form 7 January 2010

Accepted 17 March 2010

Available online 8 April 2010

Keywords:

Catalytic partial oxidation

Octane

Fuel surrogates

Rhodium

Hydrogen

Reaction mechanism

ABSTRACT

Catalytic partial oxidation of iso-octane over a rhodium/alumina coated honeycomb monolith is experimentally and numerically studied at short-contact times for varying fuel-to-oxygen ratios. A new experimental set-up with well-defined inlet and boundary conditions is presented. The conversion on the catalyst and in the gas-phase is modeled by detailed reaction mechanisms including 857 gas-phase and 17 adsorbed species. Elementary-step based heterogeneous and homogeneous reaction mechanisms are implemented into two-dimensional flow field description of a single monolith channel. Experiment and simulation provide new insights into the complex reaction network leading to varying product distribution as function of fuel-to-oxygen ratio. At fuel rich conditions, the formation of by-products that can serve as coke precursors is observed and interpreted.

© 2010 The Combustion Institute. Published by Elsevier Inc. All rights reserved.

1. Introduction

The production of hydrogen and synthesis gas (syngas, H₂ and CO) from logistic fuels such as gasoline, diesel, and kerosene by catalytic partial oxidation (CPOX) and steam reforming (SR) is currently in the focus of both academic and industrial research [1–7]. In contrast to the complex and costly supply of compressed and stored hydrogen for mobile fuel cell application, CPOX of liquid fuels allows production and utilization of hydrogen through existing routes, which, in particular, is of interest for on-board applications [8].

In the last decade, partial oxidation of a variety of gaseous and liquid hydrocarbons to syngas has been studied over rhodium-based catalysts. It was shown that many hydrocarbons contained in logistic fuels can autothermally be converted to syngas over rhodium within milliseconds at operating temperatures usually above 1000 K. Short monolithic honeycomb and foam structures made out of metal oxides usually serve as catalyst carrier. In the honeycomb structure, the noble metal is commonly impregnated into a thin alumina washcoat. No qualitative difference has been reported concerning syngas yield of foam and honeycomb based catalysts. Due to the short residence time, high fuel throughput and syngas yields can be achieved in compact reactors operated nearly adiabatically. The ignition temperature of the fuel in general decreases with

increasing molecular weight, from over 800 K to approximately 500 K for natural gas to hexadecane, respectively. Ignition of the fuel can be achieved within seconds by operating the CPOX reactor at combustion conditions initially, meaning burning of the fuel catalytically.

These features make CPOX reactors attractive for on-board supply of hydrogen and reformat fuel from conventional logistic as well as synthetic fuels, which can be integrated into auxiliary power units based on the proton exchange membrane (PEMFC) and solid oxide (SOFC) fuel cells [9]. Furthermore, the reformat gas can also serve as additive to the fuel of the internal combustion engines during cold start-up reducing the formation of nitrogen oxides (NO_x) drastically and as reducing agent for exhaust-gas after-treatment by selective catalytic reduction (SCR) of NO_x. CPOX of liquid fuels is also attractive for power generation in stationary and mobile applications at remote places due to the high energy density of the fuel as well as high electrical efficiencies and the possibility to conduct the reaction in micro reactors [10,11].

At operating temperatures around 1000 K and higher, conversion of the fuel may not only occur on the solid catalyst but also in the gas-phase. While homogeneous reactions in the fluid phase require high pressure and temperatures in CPOX of methane due to the short residence time and low reactivity [12–14], gas-phase reactions are likely for any heavier fuel at atmospheric pressure at those conditions, even for ethane and propane [15–17]. Heterogeneous and homogeneous reactions in CPOX of hydrocarbons are coupled not only by adsorption and desorption of fuel and oxygen molecules and the products, respectively, but also by adsorption and desorp-

* Corresponding author at: Institute for Chemical Technology and Polymer Chemistry, Karlsruhe Institute of Technology (KIT), Kaiserstraße 12, D-76128 Karlsruhe, Germany. Fax: +49 721 608 4805.

E-mail address: deutschmann@kit.edu (O. Deutschmann).

tion of intermediates and radicals. Therefore, mass transport of radicals and intermediates from/to the gaseous bulk phase and the catalytically active channel wall, mainly by radial diffusion in the small channels of the monolith being on the order of a quarter to 1 mm, is crucial for the interaction of heterogeneous and homogeneous reactions in CPOX reactors. In particular at transient operation, including light-off and shutdown of the reactor as well as variation of fuel composition, heat transfer effects become significant for the product composition [18]. Therefore, optimization and reliable operation of CPOX reactors call for a better understanding of the occurring complex interaction of heterogeneous and homogeneous chemical reactions as well as mass and heat transport.

Due to this complexity in chemistry and species transport, the application of detailed models for numerical simulation of CPOX reactors have been restricted to light hydrocarbon fuels such as methane and ethane [12,13,15,19]. Those models include detailed (elementary step) reaction mechanisms for heterogeneous and homogeneous chemical reactions and adequate mass and heat transport models. Such a detailed numerical simulation for CPOX of liquid fuels has not been published yet, to the best of our knowledge. However, the application of CPOX of logistic fuels for the production of hydrogen and syngas for mobile reformers crucially depends on the understanding of the formation of undesired by-products. In particular, the formation of soot precursors is likely through homogeneous gas-phase reactions at rich operating conditions and high temperatures. Even if those soot precursors may not harm the CPOX reactor, they present a potential threat for any further devices downstream such as fuel cells. The difficulties here are that the formation of soot precursors at partial oxidation and pyrolysis conditions is not completely understood yet and that the implementation of the resulting large reaction mechanism into a CFD simulation turns out to be a very formidable task.

This paper presents an experimental, modeling, and simulation study on CPOX of iso-octane over a rhodium/alumina coated honeycomb monolith. In the experimental part of this study, a recently developed experimental set-up for CPOX of liquids is used, in which well-defined inlet and boundary conditions are realized [20,21]. Even though more complex fuels have already been studied experimentally as referenced above, the single-component fuel iso-octane (i-octane, 2,2,4-trimethylpentane) has been chosen here, because it can serve as first step towards a better understanding of CPOX of logistic fuels. For this system, a detailed numerical study based on elementary homogeneous and heterogeneous chemical reaction schemes and a two-dimensional flow field description of a single monolith channel is feasible using a recently developed computer code [22–24]. The experimental and simulation results are able to explain characteristic features of CPOX of logistic fuels, which have been found for other liquid hydrocarbon fuels as well.

2. Experimental set-up and measurement procedure

2.1. Experimental set-up

Aside from measuring conversion and selectivity as functions of varying external parameters, a major objective of the experimental work here is the delivery of well-reproducible data for model development and evaluation. This implies that the reactor configuration used must guarantee well-defined initial and boundary conditions, which gave guidance to the experimental set-up. Fig. 1 gives a process flow diagram of the experimental and analytical set-up.

The liquid fuel, iso-octane, with a boiling point of 372 K (99 °C) has to be mixed rapidly below its auto ignition temperature; the same equipment is currently also used to study CPOX of much heavier hydrocarbons with boiling points up to 550 K. The development of the experimental set-up was supported by CFD simulations of the mixing process leading to a tube-in-tube configuration that allows

rapid mixing of vaporized fuels with synthetic air to feed the catalyst with a homogeneous, pulse-free mixture at a uniform temperature [20]. The higher hydrocarbons are completely evaporated before entering the tubular reactor. The fuel is stored in a pressurized tank and fed through a thermal mass flow meter (Bronkhorst LiquiFlow L23) to a three-way mixing valve where it is mixed with 0.5 standard liters per minute (slpm) of nitrogen. The liquid/inert gas mixture flows to a temperature-controlled evaporator (Bronkhorst CEM W303) ensuring complete, pulse-free evaporation. Downstream of the mixing valve, the fuel feed is calibrated by continuous gravimetric measurements using a computer assisted electronic readable balance (Sartorius-Acculab Atilon ATL323). Synthetic air and up to two additional gaseous reactants can be fed to the reactor inlet in separate lines, which are metered by thermal mass flow controllers (Bronkhorst EL Flow F201) and mixed and tempered in a pre-heater, consisting of a 6 m long steel tube. Both the reactant lines and the reactor inlet can be tempered between 340 and 600 K (70–320 °C).

The tube-in-tube inlet system is based on a modified Swagelok Ultra-Torr fitting. In the outer and inner tubes, fuel and synthetic air are provided, respectively. Through an additional support tube with an outer diameter of 6 mm, thermocouples or sampling probes can be attached to the reactor. The reactor consists of a quartz tube, 21.5 mm in inner diameter and 550 mm in length, placed inside a furnace, 350 mm in length (Carbolite HST 12/200/E301). The furnace is used for light-off of the reaction, as thermal insulation (no heating) in autothermal operation, and carbon burn-off experiments. The modified Swagelok Ultra-Torr inlet is linked to the quartz glass reactor with a Kalrez O-ring allowing temperatures up to 600 K (320 °C). The reactor outlet is sealed with a flange using a graphite gasket (Novafit), 50 mm in diameter and thermal resistance up to 820 K (550 °C).

All relevant species present in the product stream are detected by a variety of simultaneously applied analytic methods: FT-IR, MS, and a paramagnetic gas analyzer. Combination of these techniques ensures well-closed balances for carbon, hydrogen, and oxygen and permits time-resolved monitoring of at least 12 species on the order of second time-scale. Therefore, a fast screening of steady and transient states with a high quantity of data points is possible. Further carbon containing species are detected by GC-MS, however with much smaller time resolution. Typical atom balances that are reached with this combined method were between the following limits: 94% < H < 101%, 91% < C < 99% and 98% < O < 103%.

2.2. Catalyst

An industrially manufactured honeycomb catalyst (900 cells per square inch (cpsi); rhodium loading = 1.41 mg/cm³) is used. The monolith is made out of cordierite and 10 mm in length and 19 mm in diameter. The inner channel walls are coated with rhodium dispersed in an alumina washcoat; no further additives are used. The catalyst is positioned 200 mm downstream of the mixture inlet. Upstream and downstream of the catalyst, an uncoated foam monolith (γ -Al₂O₃, 85 pores per inch (ppi)) and an uncoated honeycomb monolith (600 cpsi), respectively, are placed close to the catalyst. Both non-catalytic monoliths are 10 mm in length and 19 mm in diameter and are used as heat shields and fixations for thermocouples (front face: Type K, back face: Type N).

2.3. Measurement procedure

The C/O ratio is used as parameter for the description of the composition of the mixture entering the catalyst; it is defined as the ratio of the total number of carbon atoms to the total number of oxygen atoms in the inlet mixture. The C/O ratio is varied between 0.8 and 1.2 at a constant dilution with 80 vol.% nitrogen. After light-off, the reactor is operated autothermally, that means the furnace initially

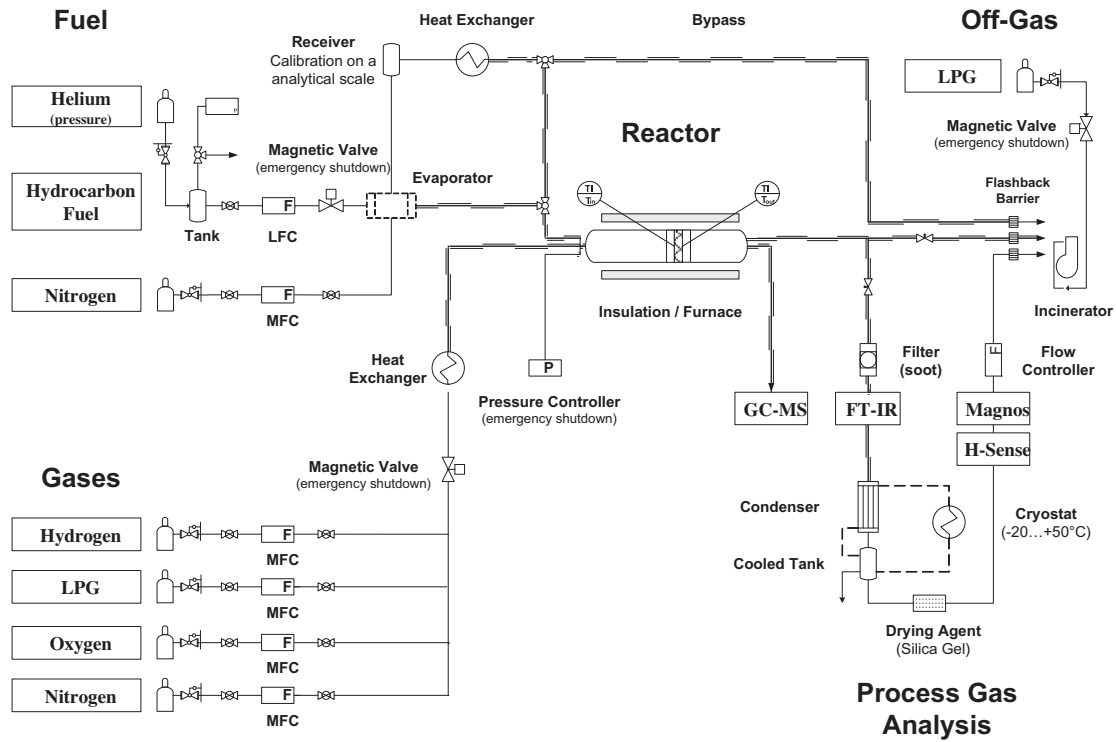


Fig. 1. Process flow diagram of the experimental set-up for the catalytic partial oxidation of higher hydrocarbon fuels.

used for light-off is switched off. A total flow rate of 4 slpm is used corresponding to a gas hourly space velocity (GHSV) of $85,000 \text{ h}^{-1}$ referred to standard conditions (298.15 K, 1013.25 mbar). Fuel and synthetic air are fed to the reactor at 463 K (190 °C).

At the reactor outlet, a part of the product stream (0.5–2.0 slpm) is directed to a process FT-IR with high-optical-throughput sampling cell (MKS Multigas 2030) in a tempered line at 418 K (145 °C). The FTIR analyzes the infrared active components CO, CO₂, H₂O, CH₄, H₂C=CH₂, CH₃-CH=CH₂, HC≡CH, H₂C=O, CH₃-CH=O with a time resolution of 0.25 Hz. The time delay between the catalyst and the spectrometer is 2–4 s, depending on the selected sampling flow rate. After cooling the product stream down to 268 K to remove high boiling liquids, the infrared inactive components H₂ and O₂ are analyzed by a sector field mass spectrometer (V&F H-Sense) and a paramagnetic gas analyzer (ABB Magnos 206), respectively. The analysis of the product stream concerning higher hydrocarbon species (C_{x>3}H_y) is performed using a GC/MS (Agilent Technologies 6890 N). After reaching steady-state, experimental data is collected for 10–15 min at each C/O ratio. No aging due to sintering or coking of the catalyst could be observed during this period. Steady states could be reached again after completing of all measurements between C/O = 0.8–2.0. No hysteresis is observed.

3. Modeling approach and numerical implementation

Due to the thermal insulation, the radial temperature gradient across the catalyst is small. Furthermore, uniform inlet conditions are ensured. Therefore, all channels of the monolith behave essentially alike, and one representative channel needs to be analyzed only. This single channel is then approximated by an axis-symmetric cylinder leading to the axial and radial spatial coordinates as independent variables of the flow field simulation. Due to the short residence time, being on the order of milliseconds, the transport in axial direction is mainly determined by convection implying that axial diffusion can be neglected, which reduces the elliptical structure of the steady-state Navier–Stokes equations to a parabolic one

by application of a boundary-layer approximation [25–27]. The resulting governing equations are a large system of parabolic partial differential equations (PDEs) with nonlinear boundary conditions arising from the coupling between the gas-phase and surface processes:

$$\text{Mass continuity : } \frac{\partial \rho u}{\partial z} + \frac{1}{r} \frac{\partial (r \rho v)}{\partial r} = 0. \quad (1)$$

$$\text{Axial momentum : } \rho u \frac{\partial u}{\partial z} + \rho v \frac{\partial u}{\partial r} = -\frac{\partial p}{\partial z} + \frac{1}{r} \frac{\partial}{\partial r} \left(\mu r \frac{\partial u}{\partial r} \right). \quad (2)$$

$$\text{Radial momentum : } 0 = \frac{\partial p}{\partial r}. \quad (3)$$

$$\text{Species continuity : } \rho u \frac{\partial Y_k}{\partial z} + \rho v \frac{\partial Y_k}{\partial r} = -\frac{1}{r} \frac{\partial (r J_{k,r})}{\partial r} + \dot{\omega}_k W_k \quad (k = 1, \dots, K_g). \quad (4)$$

$$\text{State equation : } p = \frac{\rho R T}{\bar{W}}, \quad (5)$$

$$\text{and } J_{k,r} = -D_k^m \frac{W_k}{\bar{W}} \rho \frac{\partial X_k}{\partial r}, \quad (6)$$

$$\mu = \mu(Y, T), \quad \dot{\omega}_k = \dot{\omega}_k(Y, T, p), \quad Y = (Y_1, Y_2, \dots, Y_{K_g}). \quad (7)$$

Here, z and r are the axial and radial coordinates, respectively, u and v are the axial and radial components of the velocity vector, resp., p is the pressure, T is the temperature, Y_k is the mass fraction of species k , μ is the viscosity, ρ is the mass density, c_p is the heat capacity of the mixture, λ is the thermal conductivity of the mixture, $c_{p,k}$ is the species heat capacity of the k th species, K_g is the total number of gas-phase species, $J_{k,r}$ represent the radial components of the diffusive flux vector of k th species pointing from the center to the wall, $\dot{\omega}_k$ is the rate of production of the k th species by the gas-phase reactions, h_k is the species heat enthalpy of the k th species, W_k is the molar mass of the species k , \bar{W} is the mixture mean molecular weight, and the R is the universal gas constant, D_k^m is the mixture diffusion coefficient of the k th species. The energy equation has been omitted, since only isothermal simulations were considered at this study.

At the catalytic surface, the gaseous species mass flux produced by heterogeneous chemical reactions and the mass flux of that species in the gas-phase at the gas–surface interface must be balanced, i.e.,

$$\eta F_{\text{cat/geo}} \dot{S}_k W_k = -J_{kr} \quad (k = 1, \dots, K_g), \quad (8)$$

where

$$\dot{S}_k = \sum_{i=1}^{N_s} \nu_{ik} k_{fi} \prod_{j=1}^{K_g+K_s} c_j^{\nu_{ij}^k}, \quad (9)$$

is the creation or depletion rate of gas-phase ($k = 1, \dots, K_g$) and surface ($k = K_{g+1}, \dots, K_s$) species due to the adsorption and desorption on/from the catalytic surface and reactions among surface species; K_s is the total number of adsorbed (surface) species including a vacant adsorption site species, N_s is the number of all reactions involving the catalyst; c_j are species concentrations, ν_{ik} are the stoichiometric coefficients of the reaction equations. The factor $F_{\text{cat/geo}}$ describes the ratio of catalytic active to geometric surface area, which corresponds to the amount of catalyst available for surface reactions. In this work, $F_{\text{cat/geo}}$ was experimentally determined to be 15 by CO chemisorption measurements. The effect of finite diffusion in the washcoat on the reaction rate is treated by adding an effectiveness factor, η , into the boundary conditions Eq. (8). The effectiveness factor is an algebraic expression in terms of the Thiele modulus and can be computed along with the surface reaction rates. Since the washcoat layer is thin in the monolith used here, the effectiveness factor is close to unity. More details on the impact of washcoat diffusion on mass transport in monolithic catalysts can be found, for instance, in [42].

Eq. (9) is also applied to calculate the creation or depletion rate of adsorbed species and the surface coverage, $\theta_k = ck\sigma_k/\Gamma$, with Γ and σ_k being the surface site density and the number of sites occupied by adsorbed species k , respectively. The forward rate coefficient k_{fi} of surface reaction i is calculated by a modified Arrhenius expression,

$$k_{fi} = A_i T^{\beta_i} \exp\left(-\frac{E_{ai}}{RT}\right) \prod_{k=1}^{K_s} \theta_k^{\mu_{ki}} \exp\left(\frac{\varepsilon_{ki} \theta_k}{RT}\right), \quad (10)$$

where μ_{ki} and ε_{ki} are parameters describing an additional dependence of the rate coefficients on the surface coverage [25,28].

Since we calculate the steady-state of the system, in the current study, all adsorbed species (surface species) will obey the algebraic equation system

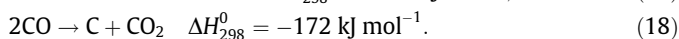
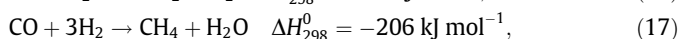
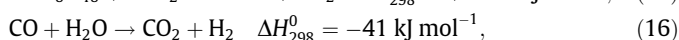
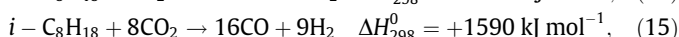
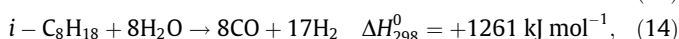
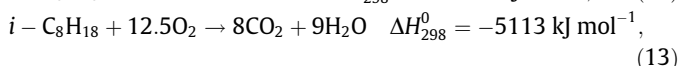
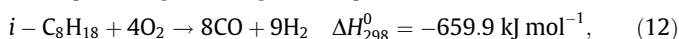
$$\dot{S}_k = 0 \quad (k = K_g + 1, \dots, K_g + K_s). \quad (11)$$

The resulting PDEs are semi-discretized by a method of lines leading to a large-scale, structured differential algebraic equation (DAE) system. The DAE system is solved using a tailored code based on the DAESOL solver using multi-step methods based on the Backward Differentiation Formula (BDF). It is a variable step size and variable order BDF code. The adaption of step size and order are controlled by error estimation. An efficient tailored method for determining consistent initial value is implemented. The recently developed code is tailored to efficiently exploit the structure of the Jacobian [22]; for more details, we refer to the user manual of the applied code DETCHEM^{CHANNEL} [24]. Using this algorithm, the new version, 2.2., of DETCHEM^{CHANNEL}, allows, for the first time to our knowledge, the solution of species equations for more than two hundred species and thousands of reactions in two phases for a two-dimensional flow problem (single catalytic monolith channel). This complexity is inherent of the CPOX of larger hydrocarbons, where a large number of intermediates and radicals are formed by a complex heterogeneous and homogeneous reaction network, which represents a challenge for detailed simulations

that should also account for the resolution of the flow field due to substantial radial diffusion effects.

4. Chemical system and reaction mechanisms

Partial oxidation of i-octane includes several other global reactions besides the direct partial oxidation Eq. (12) such as total oxidation Eq. (13), steam and dry reforming Eqs. (14) and (15), water–gas shift reaction (WGS, Eq. (16)), methanation Eq. (17), and carbon formation by the Boudouard reaction Eq. (18), reaction enthalpies are given for gaseous species:



These reactions may not only occur on the catalytic surface but also in the gas-phase due the high operating temperatures. Even though there is probably a sufficiently large number of adjustable kinetic parameters in this global reaction scheme Eqs. (12)–(18) to fit a model for representation of a set of experimental data, little insight can be gained from such a lumped mechanism. Therefore, the chemical models are based on elementary-step reaction mechanisms as much as possible in this study.

4.1. Gas-phase reaction mechanism

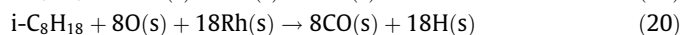
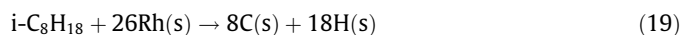
A detailed chemical kinetic mechanism developed by the combustion group at Lawrence Livermore National Laboratory (LLNL) for homogeneous oxidation of i-octane (2,2,4-trimethylpentane) is used in this study. The version of this mechanism used was published by Curran et al. [29] and developed for modeling the oxidation of i-octane in jet-stirred reactors, flow reactors, shock tubes, and CFR (Co-Operative Fuels Research) internal combustion engine for a pressure range of 0.1–4.5 MPa, a temperature range of 550–1700 K, equivalence ratios from 0.3 to 1.5, and nitrogen–argon dilution from 70% to 90%. Even though these equivalence ratios correspond to C/O ratio below 0.5, the mechanism was used without modifications for lack of alternatives.

The major steps of this mechanism are: unimolecular decomposition of fuel with H-atom abstraction, decomposition of four distinct i-octyl radicals (2,2,4-trimethyl-1-pentyl, 2,2,4-trimethyl-3-pentyl, 2,2,4-trimethyl-4-pentyl, and 2,4,4-trimethyl-1-pentyl) by C–C bond scission, isomerization by internal H-atom abstraction to other alkyl radicals, and reactions with molecular oxygen to produce peroxy – and other corresponding hydro-peroxy-alkyl radicals leading to branching reactions. The rate coefficients of these reactions depend on the type of hydrogen atom being abstracted (primary, secondary, or tertiary) and on the local environment of the H-atom. It is known that the low-temperature chemistry is very sensitive to the formation of stable olefin species from hydro-peroxy-alkyl radicals through β -scission and C–C bond breaking [29]. The proposed gas-phase mechanism consists of 7193 irreversible reactions among 857 species and is applied without any modification in the present study.

4.2. Surface reaction mechanism

The heterogeneous partial oxidation of i-octane on rhodium-based catalysts is modeled by a detailed surface reaction

mechanism for partial oxidation of C₁–C₃-species coupled with two additional “lumped” reactions for adsorption of i-octane (Eqs. (19) and (20)) assuming that i-octane adsorption quickly leads to the species that are explicitly described by the detailed part of mechanism.



Even though this rapid adsorption and destruction really is a very simplified model of the potential large numbers of intermediate steps that may occur, the fact that none of the potential intermediates C₂–C₄₊ species have been found in the gas-phase due to catalytic reactions supports the assumption of rapid destruction of the fuel molecules upon adsorption. Nevertheless, surface science studies focusing on the mechanisms of adsorption of larger hydrocarbons on noble metals are recommended. The kinetics of reactions (19) and (20) is described by a rate expression depending on temperature, i-octane gas-phase concentration, oxygen surface coverage, and number of vacant adsorption sites:

$$\dot{s}_{\text{C}_8\text{H}_{18}} = A \cdot T^\beta \exp\left(-\frac{E_a}{RT}\right) \cdot c_{\text{C}_8\text{H}_{18}}^{e_{\text{C}_8\text{H}_{18}}} \cdot c_{\text{Rh(s)}}^{e_{\text{Rh(s)}}} \cdot c_{\text{O(s)}}^{e_{\text{O(s)}}} \quad (21)$$

The kinetic parameters of Eq. (21) were adjusted by parameter optimization using the experimentally derived conversion and selectivity data; all kinetic data of the detailed mechanism were kept constant in this optimization. The kinetic parameters are given in Table 1.

A detailed surface reaction mechanism of partial oxidation of C₁–C₃ alkanes used in the simulation is derived based on our former study on the prediction of ignition, transient and steady-state operation of catalytic partial oxidation of methane over rhodium [18,30]. In the present work, this mechanism is extended by additional elementary steps for C₂- and C₃-species. The semi-empirical unity bond index-quadratic exponential potential (UBI-QEP) formalism is applied to determine the heats of adsorption of C₂/C₃-adsorbed species, reaction enthalpy changes and the activation barriers for relevant steps of the mechanism [31–33]. Kinetic parameters of reactions with C₃-species were evaluated by comparison with an experimental study on steady-state operation of partial oxidation of propane on rhodium monolith catalysts to be published on a forthcoming paper. The implementation of surface oxygenated species CHO(s) in the mechanism is crucial for the description of WGS and is supported by TPSR and TR-FTIR experiments [34]. The pre-exponential factors are either taken from literature, nominal values, or derived in this work. The nominal value for the pre-exponential factor was assumed to be: $10^{13}N_A/\Gamma$ (cm²/mol s), where N_A is Avogadro's number; 10^{13} s^{-1} is the order of magnitude of $k_B T/h$ with k_B = the Boltzmann's constant, h = Planck's constant and is the value expected from transition state theory; $\Gamma = 1.67 \times 10^{15}$ (site/cm²) – is the site density of Rh. The surface reaction mechanism consists of 56 reactions among nine gas-phase and 17 surface adsorbed species. The detailed mechanism coupled with the lumped reactions (Eqs. (19), (20)) describes all global reactions (Eqs. (12)–(18)) via a complex reaction network. The detailed mechanism is given in Table 2.

Table 1
Kinetic parameters of global reactions according to Eq. (21).

Parameter	A (mol cm s)	E _a (kJ mol ⁻¹)	β	e _{C₈H₁₈}	e _{Rh(s)}	e _{O(s)}
Reaction (19)	4.379 × 10 ⁷	6.0	0.13	0.6	1	0
Reaction (20)	7.730 × 10 ¹¹	50.0	1	1	1	1

Table 2
Surface reaction mechanism of C₁–C₃ partial oxidation over Rh.

Reaction	A (mol cm s)	E _a (kJ mol ⁻¹)
H ₂ + 2Rh(s) → 2H(s)	1.0 × 10 ^{-02a}	0.0
O ₂ + 2Rh(s) → 2O(s)	1.0 × 10 ^{-02a}	0.0
CH ₄ + Rh(s) → CH ₄ (s)	8.0 × 10 ^{-03a}	0.0
C ₃ H ₈ + Rh(s) → C ₃ H ₈ (s)	5.8 × 10 ^{-03a}	0.0
H ₂ O + Rh(s) → H ₂ O(s)	1.0 × 10 ^{-01a}	0.0
CO ₂ + Rh(s) → CO ₂ (s)	1.0 × 10 ^{-05a}	0.0
CO + Rh(s) → CO(s)	5.0 × 10 ^{-01a}	0.0
2H(s) → 2Rh(s) + H ₂	3.0 × 10 ²¹	77.8
2O(s) → 2Rh(s) + O ₂	1.3 × 10 ²²	355.2–280θ _{O(s)} ^b
H ₂ O(s) → H ₂ O + Rh(s)	3.0 × 10 ¹³	45.0
CO(s) → CO + Rh(s)	3.5 × 10 ¹³	133.4–15θ _{CO(s)} ^b
CO ₂ (s) → CO ₂ + Rh(s)	1.0 × 10 ¹³	21.7
CH ₄ (s) → CH ₄ + Rh(s)	1.0 × 10 ¹³	25.1
C ₃ H ₈ (s) → C ₃ H ₈ + Rh(s)	1.0 × 10 ¹³	30.1
C ₃ H ₈ (s) + Rh(s) → C ₃ H ₇ (s) + H(s)	3.7 × 10 ²¹	55.0
C ₃ H ₇ (s) + H(s) → C ₃ H ₈ (s) + Rh(s)	3.7 × 10 ²¹	56.6
C ₃ H ₇ (s) + Rh(s) → C ₃ H ₆ (s) + H(s)	3.7 × 10 ²⁴	73.4
C ₃ H ₆ (s) + H(s) → C ₃ H ₇ (s) + Rh(s)	3.7 × 10 ²¹	75.9
C ₃ H ₆ (s) + O(s) → C ₃ H ₇ (s) + OH(s)	1.7 × 10 ²⁴	71.5
C ₃ H ₇ (s) + OH(s) → C ₃ H ₈ (s) + O(s)	3.7 × 10 ²¹	31.3
C ₃ H ₇ (s) + O(s) → C ₃ H ₆ (s) + OH(s)	3.7 × 10 ²⁴	88.7
C ₃ H ₆ (s) + OH(s) → C ₃ H ₇ (s) + O(s)	3.7 × 10 ²¹	45.3
C ₃ H ₆ (s) + Rh(s) → C ₂ H ₃ (s) + CH ₃ (s)	3.7 × 10 ²⁴	83.7
C ₂ H ₃ (s) + CH ₃ (s) → C ₃ H ₆ (s) + Rh(s)	3.7 × 10 ²¹	55.8
C ₂ H ₃ (s) + Rh(s) → C(s) + CH ₃ (s)	3.7 × 10 ²¹	35.6
C(s) + CH ₃ (s) → C ₂ H ₃ (s) + Rh(s)	3.7 × 10 ²¹	118.7
CH ₄ (s) + Rh(s) → CH ₃ (s) + H(s)	3.7 × 10 ²¹	61.0
CH ₃ (s) + H(s) → CH ₄ (s) + Rh(s)	3.7 × 10 ²¹	51.0
CH ₃ (s) + Rh(s) → CH ₂ (s) + H(s)	3.7 × 10 ²⁴	103.0
CH ₂ (s) + H(s) → CH ₃ (s) + Rh(s)	3.7 × 10 ²³	44.1
CH ₂ (s) + Rh(s) → CH(s) + H(s)	3.7 × 10 ²⁴	100.0
CH(s) + H(s) → CH ₂ (s) + Rh(s)	3.7 × 10 ²¹	68.0
CH(s) + Rh(s) → C(s) + H(s)	3.7 × 10 ²¹	21.0
C(s) + H(s) → CH(s) + Rh(s)	3.7 × 10 ²¹	172.8
CH ₄ (s) + O(s) → CH ₃ (s) + OH(s)	1.7 × 10 ²⁴	80.3
CH ₃ (s) + OH(s) → CH ₄ (s) + O(s)	3.7 × 10 ²¹	24.3
CH ₃ (s) + O(s) → CH ₂ (s) + OH(s)	3.7 × 10 ²⁴	120.3
CH ₂ (s) + OH(s) → CH ₃ (s) + O(s)	3.7 × 10 ²¹	15.1
CH ₂ (s) + O(s) → CH(s) + OH(s)	3.7 × 10 ²⁴	114.5
CH(s) + OH(s) → CH ₂ (s) + O(s)	3.7 × 10 ²¹	36.8
CH(s) + O(s) → C(s) + OH(s)	3.7 × 10 ²¹	30.1
C(s) + OH(s) → CH(s) + O(s)	3.7 × 10 ²¹	136.0
H(s) + O(s) → OH(s) + Rh(s)	5.0 × 10 ²²	83.7
OH(s) + Rh(s) → H(s) + O(s)	3.0 × 10 ²⁰	33.7
H(s) + OH(s) → H ₂ O(s) + Rh(s)	3.0 × 10 ²⁰	33.5
H ₂ O(s) + Rh(s) → H(s) + OH(s)	5.0 × 10 ²²	106.4
OH(s) + OH(s) → H ₂ O(s) + O(s)	3.0 × 10 ²¹	100.8
H ₂ O(s) + O(s) → OH(s) + OH(s)	3.0 × 10 ²¹	171.8
C(s) + O(s) → CO(s) + Rh(s)	5.2 × 10 ²³	97.9
CO(s) + Rh(s) → C(s) + O(s)	2.5 × 10 ²¹	169.0
CO(s) + O(s) → CO ₂ (s) + Rh(s)	5.5 × 10 ¹⁸	121.6
CO ₂ (s) + Rh(s) → CO(s) + O(s)	3.0 × 10 ²¹	115.3
CO(s) + H(s) → HCO(s) + Rh(s)	5.0 × 10 ¹⁹	108.9
HCO(s) + Rh(s) → CO(s) + H(s)	3.7 × 10 ²¹	0.0 + 50θ _{CO(s)} ^b
HCO(s) + Rh(s) → CH(s) + O(s)	3.7 × 10 ²⁴	59.5
CH(s) + O(s) → HCO(s) + Rh(s)	3.7 × 10 ²¹	167.5

The mechanism will be available on www.detchem.com.

^a Value initial sticking coefficient.

^b Coverage dependence applied so that the reaction scheme remains thermodynamically consistent nomenclature given in [11].

5. Results and discussion

5.1. Two reaction zones

The numerical simulation predicts the two-dimensional flow and concentrations profiles in the fluid phase inside a single channel of the monolithic catalyst as well as the coverage on the catalytic surface as function of axial position. First simulations revealed that all major products (H₂, CO, H₂O, and CO₂) are heterogeneously produced within the first section of the catalyst starting at the

front face of the catalyst and having an approximate length of 1 mm (depending on the C/O ratio). This principal behavior is illustrated in Fig. 2 for C/O ratio of 1.0, which is stoichiometric for syngas production. Here, the hydrogen and oxygen profiles clearly reveal that the reactor is operated in a mass-transfer-limited regime. Even for the fast diffusing hydrogen species, strong radial gradients can be recognized in the channel of 0.92 mm diameter. Close to the surface, significant amounts of oxygen are only available at the front face of the catalyst. Mass-transfer of oxygen from the bulk fluid to the catalytic channel wall limits the overall reaction rate. We carried out experiments with monoliths of different rhodium loadings and the corresponding simulations with varying $F_{\text{cat}/\text{geo}}$. Both experiment and simulation do not show a substantial decrease of hydrogen yield as long as the amount of rhodium exceeds a critical (low) value agreeing with findings of former studies [35]. Hence, all experimental results support the conclusion of a mass-transfer limited reactor behavior at the catalyst entrance.

Furthermore, the concentrations of these species remain almost constant in the remainder of the channel, where some homogeneous conversion of the remaining fuel occurs in the gas-phase. Therefore, the reactor can be divided into two axial zones: (1) In approximately 1 mm long heterogeneous reaction zone, homogeneous reactions do not need to be considered. Conversion almost exclusively occurs on the surface. The residence time of less than one millisecond (0.7 ms at C/O = 1.0) in that zone is far too short to lead to a radical pool large enough for initiation of gas-phase conversion. Aside from that, most of the radicals are also quenched on the catalytic surface. (2) In a second zone, starting at an axial position, where oxygen is already completely consumed at the gas–surface interface, the surface kinetics slows down as discussed below and homogeneous reactions may become significant. At rich conditions, it may even be the case that in the second, much longer zone, gas-phase chemistry only matters and heterogeneous conversion can be neglected. This separation of a short-contact time reactor for CPOX of higher hydrocarbons into two zones was already proposed and applied by Panuccio et al. [36] without having the numerical tools for proving that separation by coupled models. The difference in the present study is that the heterogeneous model is used over the entire channel length taking into account the interaction between gas-phase and surface reactions, also when homogeneous conversion has started.

CPOX of hydrocarbons in short-contact time reactors is known to show a temperature peak in the catalyst entrance zone, in general around the position where most of the oxygen is consumed; further downstream the temperature usually drops slightly due

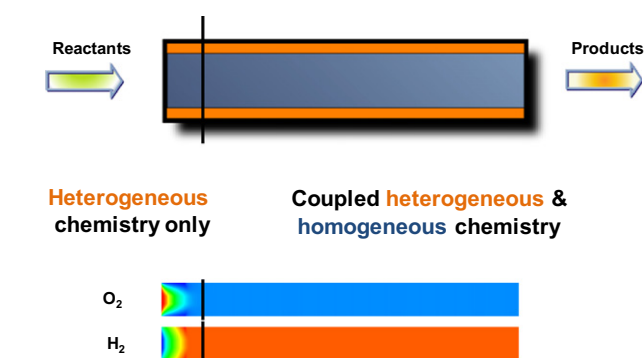


Fig. 2. Sketch of the single channel simulated and the general behavior in the reactor (upper panel); simulated hydrogen and oxygen profiles shown for C/O = 1.0 (lower panel; the blue color denotes the minimum of zero mole fraction, the red color the maximum of 0.16 and 0.24 mol fraction for oxygen and hydrogen, respectively). (For interpretation of the references to color in this figure legend, the reader is referred to the web version of this article.)

to endothermic reforming reactions [18,37–39]. We observed a similar temperature profile for CPOX of *i*-octane in our simulations when a heat balance was included. Since those simulations are extremely intensive when coupled with large homogeneous reaction schemes and the focus of the current study is on the interaction of heterogeneous and homogeneous reactions, we assumed isothermal conditions for the simulations discussed in the remainder. The simulations now use the experimentally determined back-face temperature as operating reactor temperature of the catalytic monolith as given in Fig. 3. This temperature decreases from 1350 K at C/O = 0.8–1070 K at C/O = 1.2. It should be mentioned that the computed adiabatic exit temperature based on the reactant inlet temperature of 463 K (190 °C) and composition and the measured outlet temperature leads to a temperature that is 20–70 K and 70–120 K higher than the measured back-face temperature for the C/O ranges of 1.2–1.0 and 1.0–0.8, respectively.

5.2. Major products and reactor temperature at varying C/O ratios

Oxygen is completely converted at all conditions studied, while conversion of the fuel strongly depends on the C/O ratio as shown in Fig. 4. In Fig. 4, the experimentally determined concentrations of the major products H₂, CO, H₂O, and CO₂ are given as function of the C/O ratio varied between 0.8 and 2.0, i.e., from lean to rich conditions related to the stoichiometric formation of syngas at C/O = 1.0 Eq. (12). The C/O ratio really determines selectivity and conversion in catalytic partial oxidation of *i*-octane on rhodium, two distinct regions can be recognized. At fuel lean and stoichiometric conditions (up to C/O = 1.0) full conversion of *i*-octane is reached (Fig. 3). Experimentally, no fuel or any other hydrocarbon compounds can be detected with FT-IR or GC-MS for fuel lean conditions C/O below 0.9 (detection limit <10 ppm). At fuel rich conditions (C/O > 1) the amount of oxygen is too little for full conversion of the fuel to syngas. Here the fuel conversion continuously drops to 57% at C/O = 2.

Since increasing C/O ratio obviously leads to a decrease of the amount of fuel that is (partially and totally) oxidized, the reactor temperatures decrease with increasing C/O ratio (Fig. 3) but stabilizes at approximately 1023 K (750 °C) at C/O = 1.2. This behavior coincides with the rate of total oxidation products. At lean conditions, H₂O and CO₂ selectivities are as high as 23.1% and 12.6%, respectively, at C/O = 0.8 leading to a catalyst exit temperature of as much as 1373 K (1100 °C) (Fig. 3). With increasing C/O ratio, the selectivities, S_i , and even yields, Y_i , of the total oxidation prod-

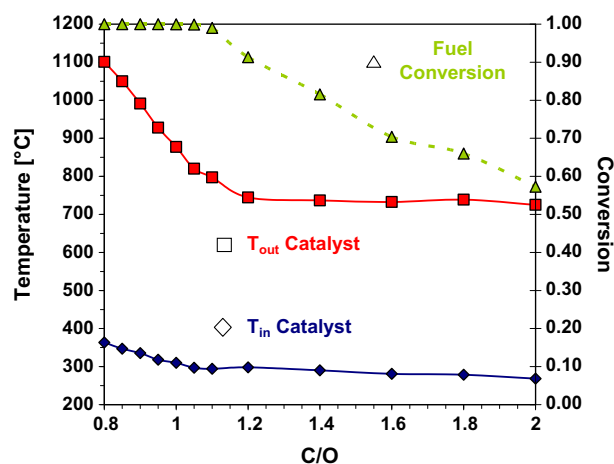


Fig. 3. Measured gas temperature at the catalyst inlet and back face (left) and fuel conversion (right) as function of C/O ratio for CPOX of *i*-octane over Rh.

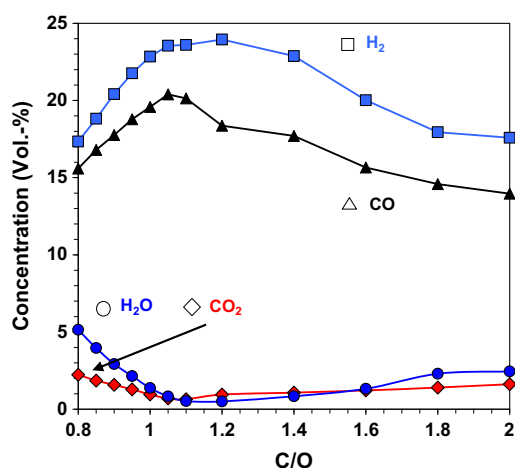


Fig. 4. Experimentally determined concentration of the major products of CPOX of *i*-octane over Rh as a function of C/O ratio.

ucts drop continuously to values of $S_{\text{H}_2\text{O}} = 1.9\%$, $S_{\text{CO}_2} = 4.2\%$, $Y_{\text{H}_2\text{O}} = 1.7\%$, $Y_{\text{CO}_2} = 4.6\%$ to reach a minimum at $C/O \sim 1.2$. For higher C/O ratios, the amount of both total oxidation products increases again. Since both fuel and oxygen are consumed completely at lean conditions ($C/O < 1$), the temperature directly corresponds to the stoichiometric composition and kinetic and thermodynamic effects are basically not significant, that means the fact that lower temperatures favor total oxidation over partial, such that the latter does not play a role. However, at rich conditions ($C/O > 1$), a more complex behavior occurs. Here, the less available oxygen favors partial oxidation from a stoichiometric point of view. However, the decreasing temperature favors total oxidation from a thermodynamic point of view. Hydrogen selectivity as function of temperature and C/O ratio at thermodynamic equilibrium, given in Fig. 8, reveals that the impact of temperature on hydrogen selectivity is stronger at $C/O > 1$ for a given C/O ratio in the relevant temperature range above 973 K (700 °C). Selectivity towards total oxidation increases again at $C/O > 1.2$ and the temperature remains almost constant at approximately 1023 K (750 °C). The measured hydrogen selectivity is significantly higher than the one expected in thermodynamic equilibrium. This behavior is not contradictory to the reaction sequence, first mainly total oxidation and then mainly reforming and hydrogen production, because *iso*-octane conversion strongly decreases with increasing C/O and therefore the system is still far away from thermodynamic equilibrium. At $C/O < 1.2$, thermodynamics would favor higher hydrogen selectivity due to higher temperatures with decreasing C/O ratio. However, the larger amount of oxygen available leads to significant CO_2 formation first, and CO_2 reforming is a very slow process; hence the hydrogen selectivity decreases.

The increasing amount of by-products with increasing C/O ratio discussed below also has a minor influence on the temperature and consequently also on the yields at $C/O > 1$, which slightly introduces kinetic effects in this discussion on temperature and overall conversion towards the major products.

It should be noted that homogeneous reaction rates are also very sensitive to temperature, which means the product distribution due to homogeneous conversion will not only depend on the C/O ratio but also on the temperature related to the varying C/O ratio. Due to the thoroughly metering and mixing of fuel and oxygen up, homogeneous reactions can be excluded upstream the catalyst. In reference experiments with non-catalytic monoliths, decomposition of fuel was not observed, neither in the reactor inlet nor in the monolithic section and downstream at the given inlet temper-

atures up to 573 K (300 °C). Further discussion on the impact of gas-phase chemistry is given in Section 5.5.

The best H- and C-based selectivity for hydrogen and carbon monoxide production, respectively, can be achieved at $C/O \sim 1$, being 94% for both H_2 (Fig. 5) and CO (not shown). It is noted that the maximum of syngas yields does not always corresponds exactly to the stoichiometric ratio in CPOX of heavy hydrocarbons [21]. At lower C/O ratios, the amount of the total combustion products, CO_2 and H_2O , continuously increases but no other products are observed aside from the syngas. As the C/O ratio is increased above stoichiometric composition, the selectivity towards hydrogen and carbon monoxide decreases and the selectivity for olefins ($\text{C}_2\text{--}\text{C}_4$) increases (Figs. 5–7). The selectivity for CO_2 remains below 4% for all $C/O > 1$.

5.3. Formation of by-products at $C/O > 1$

The C-based selectivity and yield of the individual major by-products, methane, ethylene, propylene, acetaldehyde, and *iso*butylene, are displayed as a function of C/O ratio in Fig. 6, detailed information on concentrations is given in Fig. 7. All those by-products play a significant role as coke and soot precursors and, hence, are crucial to understand coke formation in those reactors. Note, that acetaldehyde is the only observed oxygenated hydrocarbon cracking product. Its maximum carbon based yield does not exceed 1% even under fuel rich operation conditions of $C/O = 2.0$. In con-

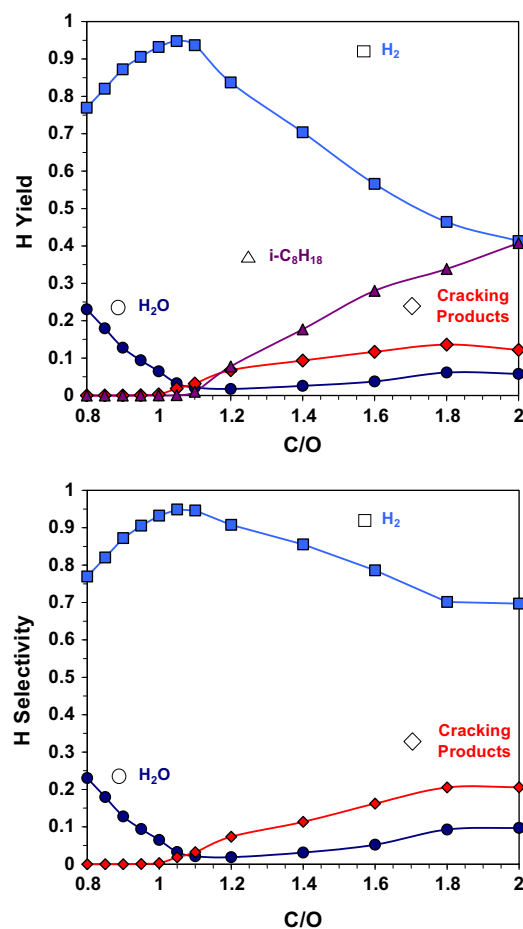


Fig. 5. Experimentally determined H-based yield (top) and selectivity (bottom) in CPOX of *i*-octane over Rh as function of C/O ratio. Cracking products denotes the sum of all hydrocarbons contained in the products stream except the fuel that is given separately ($i\text{-C}_8\text{H}_{18}$).

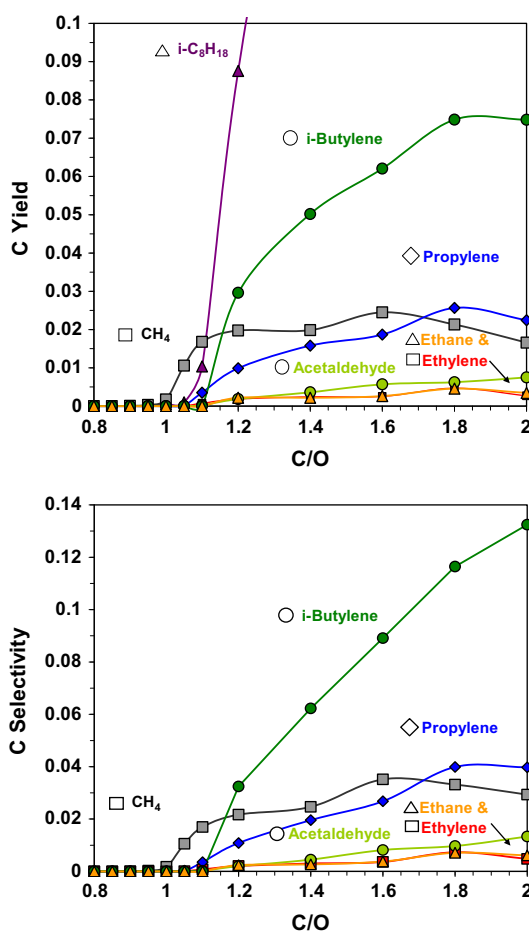


Fig. 6. Experimentally determined C-based yield (top) and selectivity (bottom) in CPOX of i-octane over Rh as a function of C/O ratio. The amount of unconverted fuel is expressed as yield ($i\text{-C}_8\text{H}_{18}$ in top figure).

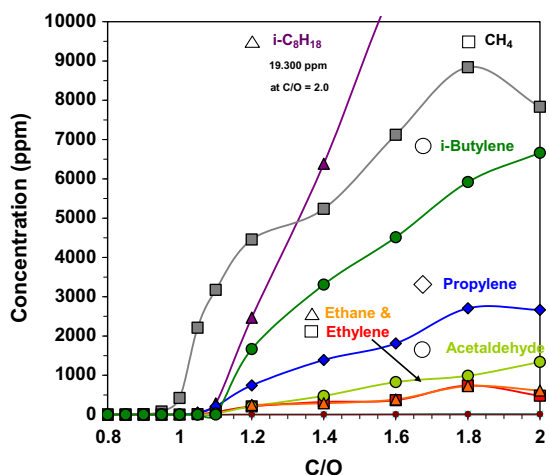


Fig. 7. Experimentally determined concentrations of the side-products and the fuel remaining in the outlet stream of CPOX of i-octane as a function of C/O ratio.

trast to the production of other cracking products, the formation of methane is not coupled with a breakthrough of the fuel.

Based on concentration (Fig. 7), methane dominates the by-products under stoichiometric reaction conditions followed by i-butylene, propylene, and ethylene. Under more fuel rich condi-

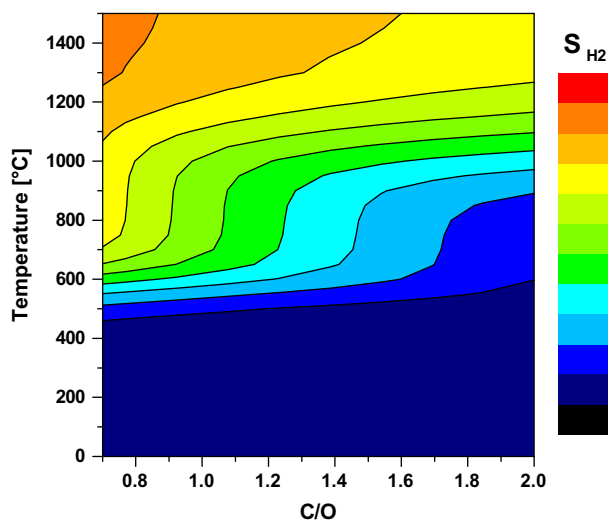


Fig. 8. H_2 -Selectivity as function of temperature and C/O ratio for i-octane/oxygen mixtures at thermodynamic equilibrium.

tions, the olefins, in particular i-butylene, reach C-based selectivities of even more than 10% at $\text{C/O} > 1.8$ (Fig. 6). Thermodynamic equilibrium calculations at these conditions predict higher methane concentrations. However, the equilibrium composition will not be reached yet within the millisecond contact time applied in the reactor. In the experiment, the formation of carbonaceous species or carbon layer at rich conditions is observed on the catalyst and further downstream on the quartz tube walls. Below $\text{C/O} = 1$, no olefins are detected at all.

5.4. Catalytic reaction kinetics and interaction with mass transport

The experimental set-up used is only able to analyze the chemical composition of the flow field at the reactor outlet that means the product composition. However, for a more detailed understanding the spatial profiles inside the catalyst is of great interest. Here, we make use of the modeling and simulation tools developed. Figs. 9 and 10 reveal the numerically predicted two-dimensional species profiles of the reactants, i-octane and oxygen, and all major products within a single catalyst channel, 0.92 mm in diameter, at C/O ratio of 0.8 and 1.2, respectively. The profiles were computed at isothermal conditions with operating temperatures of 1359 K and 1076 K, respectively. At both C/O ratios, the qualitative reaction analysis reveals two similar main features:

- (1) The catalytic surface reaction rate is very fast in the entrance region. Even though the channel diameter is small, strong radial gradients are formed in that 1 mm long first region of the catalyst. Here, the concentrations of both reactants, at the gas–surface interface almost vanish, that means the overall catalytic reaction is clearly mass-transfer limited. Radial diffusion really matters and therefore, any modeling approach needs to account for radial mass transfer in the single channel what is frequently not considered in literature. Additionally, the different diffusion coefficients of the individual species matter; for instance radial profiles of the hydrogen mole fractions are much smaller in comparison with those of CO due to the higher diffusion coefficient of hydrogen.
- (2) As long as some oxygen is available on the surface, total oxidation occurs on the surface. The major products are steam and carbon dioxide in the first tenths of a millimeter of the catalyst. In particular, high amounts of H_2O are present close to the surface forming strong radial gradients; this effect is

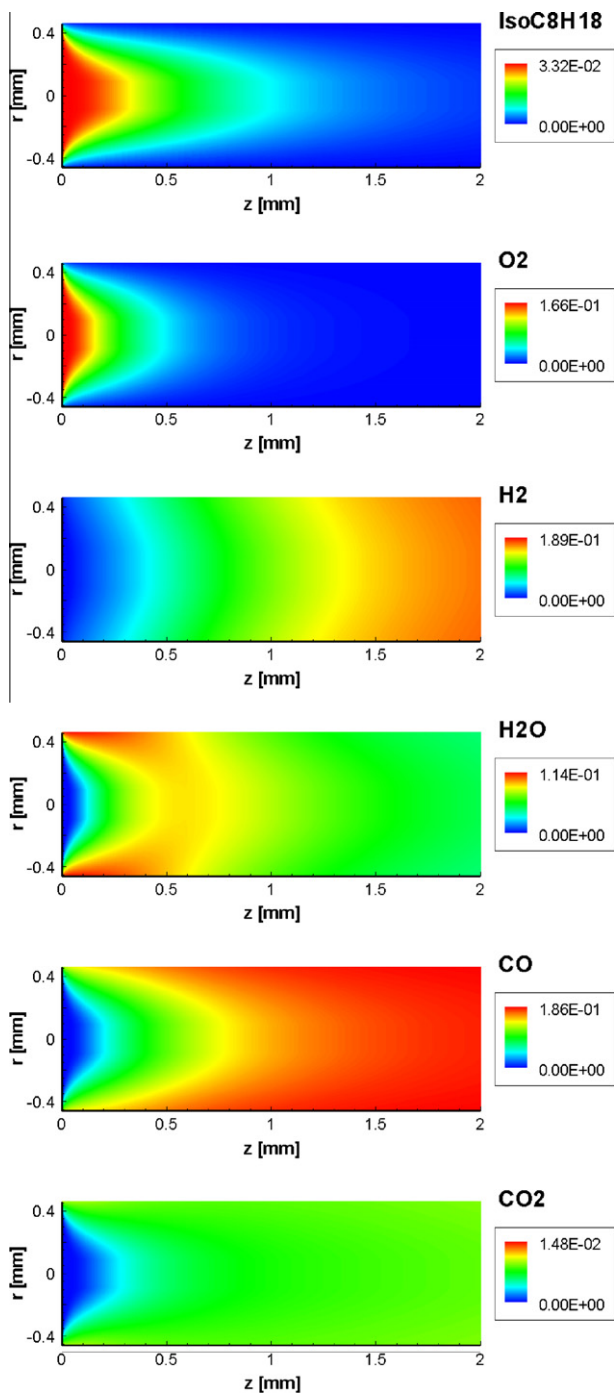


Fig. 9. Numerically predicted profiles of molar fractions of reactants and major products in the entrance region of the catalyst at $C/O = 0.8$. Flow direction is from left to right.

more pronounced for $C/O = 0.8$, because much more total oxidation occurs at those conditions compared with the case of $C/O = 1.2$. There is basically no hydrogen formed in the entrance region of the catalyst, at least as long as oxygen is available in the gas-phase close to the surface. Further downstream, the steam concentration decreases again. In that same region, hydrogen formation begins. Consequently, partial oxidation of *i*-octane to synthesis gas rather follows an indirect reaction path than a direct reaction path: first total oxidation occurs, then the remaining fuel is converted to syngas by steam reforming. This behavior has been seen before in CPOX of light hydrocarbons [18,30,38].

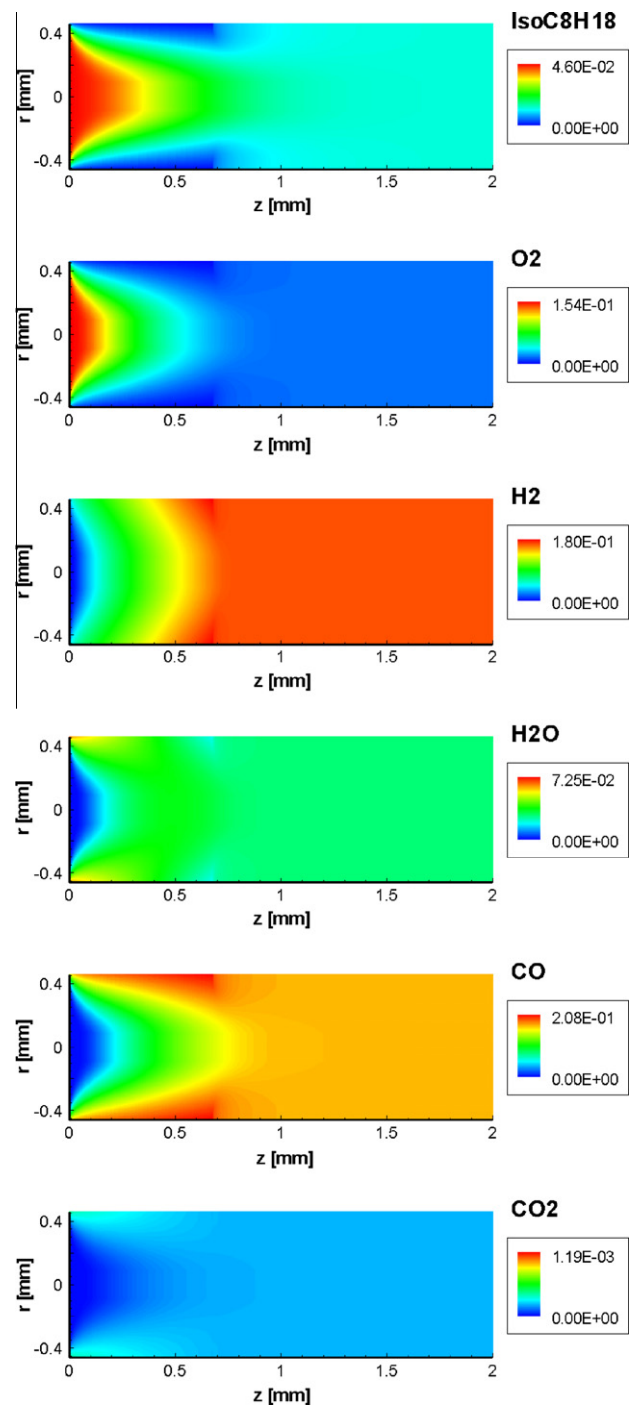


Fig. 10. Numerically predicted profiles of molar fractions of reactants and major products in the entrance region of the catalyst at $C/O = 1.2$. Flow direction is from left to right.

There are two minor but significant difference between lean and rich conditions analyzing the species profiles of the major products:

- (1) The zone of total oxidation is significantly smaller at rich conditions and consequently more hydrogen is formed in the first millimeter of the catalyst. The stronger radial H_2 and CO gradients for $C/O = 1.2$ are related to this very fast catalytic reaction rate.

(2) While the reaction proceeds along the reactor at lean conditions, even though at a declining rate, the formation of all major products seems to stop at an axial position of $z \sim 1$ mm for the case of $C/O = 1.2$. This behavior will be discussed in more detail in the next sections.

It should be noted that, for all C/O ratios, the variation of all species profiles of the reactants and all four major products downstream $z = 2$ mm is rather small and all radial profiles disappear.

5.5. Homogeneous reactions in the gas-phase

It is well known that homogeneous gas-phase reactions are significant in catalytic partial oxidation of light hydrocarbons over noble metals, even at the short-contact times of milliseconds and at atmospheric pressure except for methane [13,15–17,40]. Therefore, it is expected that reactions in the gas-phase may also overlap with the catalytic conversion in CPOX of *i*-octane. In the present study, a very detailed homogeneous reaction mechanism was coupled with the catalytic reaction scheme as discussed above.

The simulation here reveals that in the lean regime, $C/O = 0.8$, gas-phase reactions do not contribute to the overall conversion. Even though the high reactor temperature of 1373 K (1100 °C) occur at those lean conditions and a significant surface reaction rate can still be observed in the middle section ($z > 1$ mm) of the catalyst, simulation with and without the gas-phase reaction model do not reveal any difference in the species profiles. This behavior can be understood by the fact that the radicals formed in the gas-phase quickly diffuse to the catalytic surface where they adsorb with high probability and recombine. The catalytic surface consequently acts as sink for radicals and inhibits the formation of a radical pool large enough to initiate significant conversion in the gaseous fluid phase. At lean conditions, the model predicts low surface coverage of the catalyst by adsorbed species (denoted by $Rh(s)$ in Fig. 12 top) except in the entrance region, that means there are enough vacant surface sites available for adsorption and recombination of radicals. At the entrance of the catalyst, the surface major adsorbed species is oxygen, $O(s)$; in this region total oxidation occurs and all the water is formed. Further downstream, oxygen on the surface originates from re-adsorbed water only and the oxygen coverage is smaller by several orders of magnitude. Since the few millisecond residence time in the first millimeter of the catalyst is too short to initiate a sufficiently large radical pool, no gas-phase conversion occurs along the entire catalytic section of the reactor. It should be reminded, that, at lean conditions, no side-products such as olefins are formed and coking is not observed, neither on the catalyst nor in the downstream monolith and exhaust channel.

However, at rich conditions ($C/O > 1$), an increasing amount of side-products is formed and the catalyst as well as the downstream uncoated monolith and the exhaust line are covered with a carbon layer (coke). It was already discussed that there is basically no fuel conversion on the catalyst in the downstream catalyst section of $z > 1$ mm at $C/O = 1.2$. However, as shown in Fig. 11, the formation of side-products begins in this area. The typical coke precursors ethylene, propylene, and acetylene are formed in this region. Aside from that methane production occurs in this downstream section. Furthermore, no radial gradients of species profiles of the products and intermediate radicals (HO_2 and CH_3 in Fig. 11) are formed in the simulation including gas-phase chemistry. Computed and experimentally determined product concentrations of ethylene, propylene, acetylene, and methane agree qualitatively well within the given simplifications such as isothermal reactor conditions, neglected interaction of gas-phase species with coke layer as discussion below. Larger quantitative deviations between experiment and model are de-

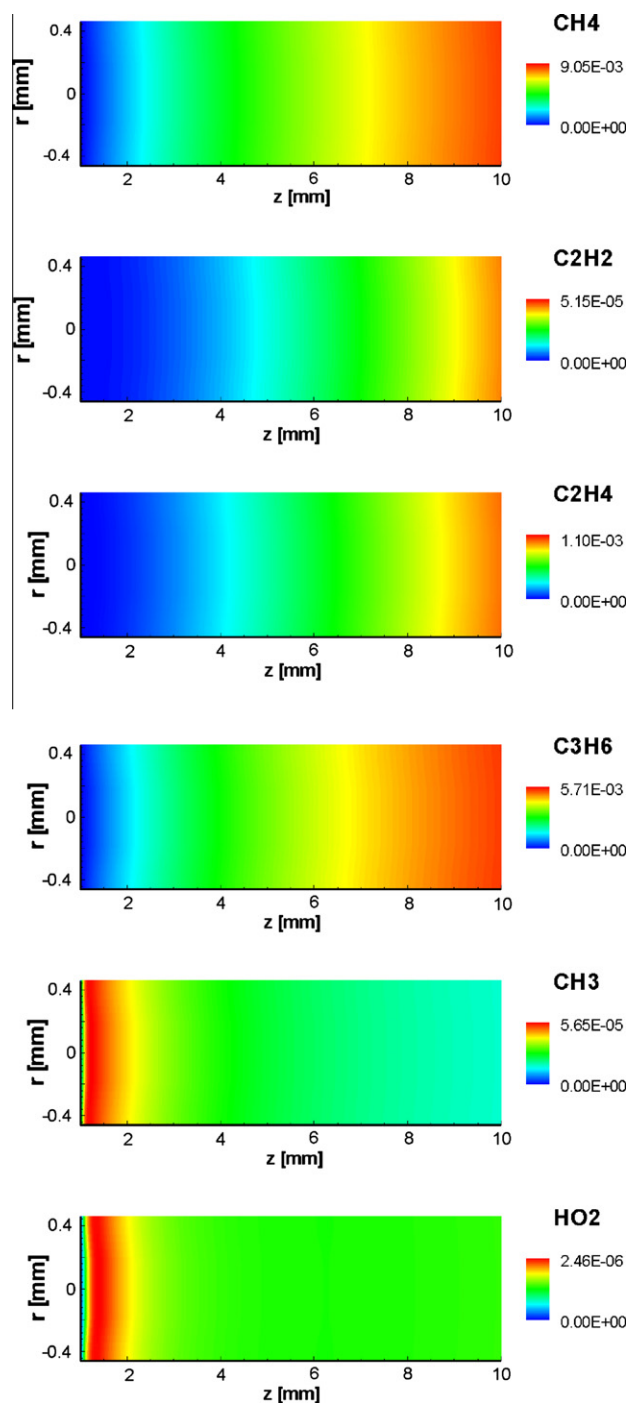


Fig. 11. Numerically predicted profiles of molar fractions of minor products and radicals along the entire catalyst at $C/O = 1.2$. Flow direction is from left to right.

tected for *i*-butylene and acetaldehyde concentrations. The experimentally determined vs. computed outlet mole fractions for the case of interest here ($C/O = 1.2$) are: C_2H_4 : 6.4×10^{-4} vs. 9.6×10^{-4} , C_3H_6 : 1.5×10^{-3} vs. 4.0×10^{-3} , CH_4 : 9.9×10^{-3} vs. 9.1×10^{-3} , *i*- C_4H_8 : 1.5×10^{-3} vs. 6×10^{-3} . Potential homogeneous conversion in the gas-phase downstream the catalyst may add to the difference. Note that the gas-phase chemistry model is taken from literature without any modification.

Summarizing, homogeneous gas-phase reactions lead to the formation of methane, olefins, acetylene, and other cracking products with a C-based selectivity of up to 20% at rich conditions.

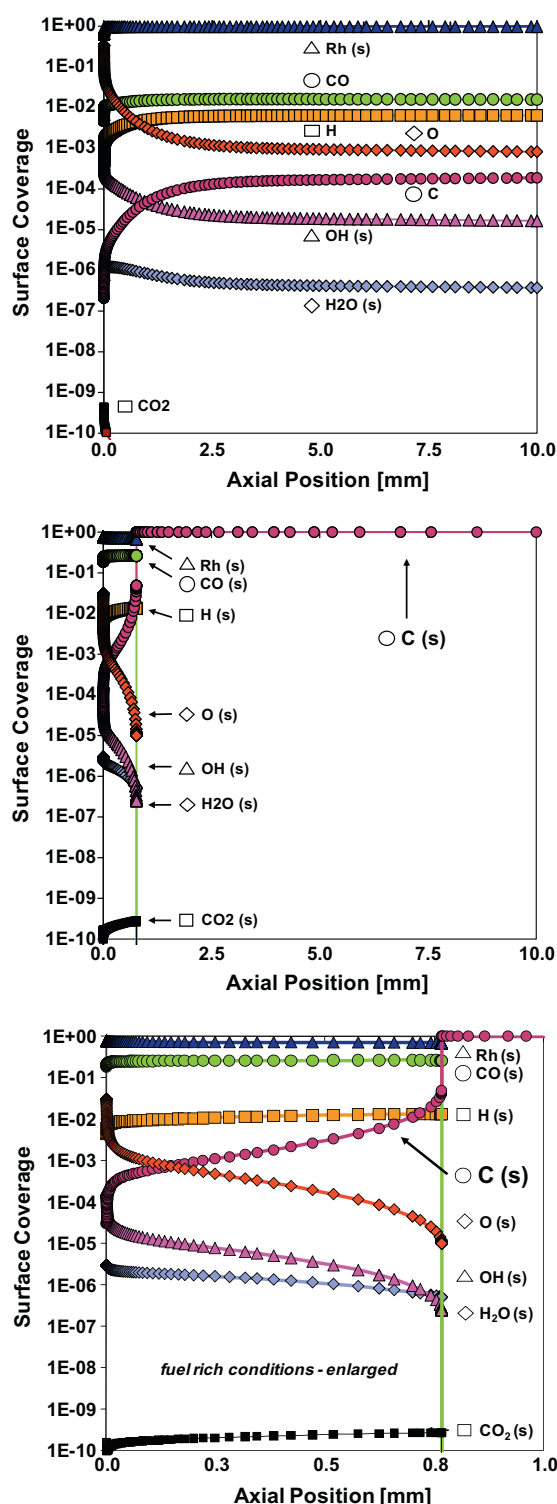


Fig. 12. Numerically predicted surface coverage as a function of axial position along the monolith channel: C/O = 0.8, 1359 K (top), C/O = 1.2, 1076.3 K (bottom).

5.6. Coke formation

The model predicts surface coverages of the catalyst with adsorbed species as function of axial position in the reactor, which is given for two example cases in Fig. 12. At rich conditions, the model predicts a completely carbon, C(s), covered surface downstream of the catalyst, $z > 1$ mm. In this region, the catalyst is basi-

cally inactive. Since the model does not include interactions between gas-phase species and carbon on the surface directly, the gas-phase conversion practically proceeds independent of any direct influence of the catalytic surface that means radicals are not recombined on the surface for $z > 1$ mm. However, both heterogeneous and homogeneous chemistry are coupled, because the resulting carbonaceous over-layer on the catalyst is a result of the gas-phase species concentrations near the channel wall. The exact position of this C(s) layer is rather sensitive to small variations of several physical parameters such as reactor temperature, catalyst loading, flow rate, diffusion models but always occurs in the first third of the catalyst at given C/O ratio and is very typical for the rich regime.

The catalytic monolith shows a very similar behavior after operation at rich conditions. The picture in Fig. 13 taken of the catalyst after operation at C/O = 1.2 clearly reveals that the downstream part of the catalyst is covered with a layer of coke. The exact position of the onset of the coking layer of course varies from channel to channel a bit due to local variations in catalyst loading and other parameters, also given hints for the oversimplifications in the model assumptions ("every channel basically is alike"). At lean conditions, such a coke formation is not observed.

Both experiment and simulation reveal fast adsorption and destruction of i-octane on rhodium at the beginning of the monolith channel, which leads to the formation of carbonaceous species or carbon layer at rich conditions after consumption of rate limiting oxygen. This inhibition effect prevents or at least drastically slows down further adsorption and reaction of hydrocarbons and intermediates on the surface and, therefore, more fuel is available for homogeneous conversion. An accurate prediction of the position where the transition to an almost fully carbon-covered surface occurs is very difficult. This position is also highly sensitive to the kinetic parameters. Furthermore, the surface reaction mechanism does not include a model for the formation of multiple carbon layers and other "coke" structures possibly formed such graphene layers, graphite, and whiskers. In the simulation, the formation of the carbon layer is predicted slightly further upstream than it can be observed by investigation of the splitted catalyst after experiments under fuel rich conditions (C/O = 1.2). Consequently, predicted conversion of i-octane decreases faster than experimentally measured with increasing C/O ratio. However, it is noted that coking of the downstream section of catalyst is also observed experimentally at rich conditions after half an hour of operation. Coking is a transient phenomena but the simulation are carried out for steady-state conditions, that means that the final position of the onset of coking may still move upstream with time of operation, even though it may finally be stabilized at the position, at which the gaseous oxygen concentration in the gas-surface-interface reaches a critical low value.



Fig. 13. Photo taken from a catalytic monolith removed from the reactor after operation C/O = 1.2. The inlet flow enters the catalyst from the left side.

In particular, the olefins formed in the gas-phase at rich conditions have a high potential to form soot particles further downstream of the catalyst, because it will be difficult to cool-down fast enough the hot product to avoid any further gas-phase reactions and molecular growth will occur [41]. The formed particulates definitely are a threat for any other devices such as fuel processing systems and fuel cells, which are located downstream of the CPOX reactor. Adequate measures have to be taken to avoid either operation of the CPOX reactor in a regime where gas-phase reactions are likely to produce precursors of particulate matter, to reduce olefin concentrations with post-catalyst conversion strategies, or to collect the particles formed, e.g. by the filters.

6. Conclusions

This combined experimental, modeling and simulation study led to a much better understanding of the internal processes in catalytic partial oxidation of iso-octane over rhodium coated monolithic catalyst. A recently set-up laboratory-scale reactor with the associated analysis was used to provide a fundamental data basis, in particular revealing the effect of the C/O ratio on conversion, selectivity, and the formation of soot precursors. Two-dimensional simulations of the flow field in the single catalytic channels coupled with detailed models for heterogeneous and homogeneous fuel conversion can substantially support the understanding of the complex interaction of catalytic and gas-phase reactions as well as mass transport in short-contact times reactors for the catalytic partial oxidation of larger hydrocarbons over noble metals.

Very high hydrogen and carbon monoxide selectivity was found at stoichiometric conditions ($C/O = 1$), while at lean conditions more total oxidation occurs. At rich conditions ($C/O > 1$), homogeneous chemical conversion in the gas-phase is responsible for the formation of by-products such as olefins that also have the potential for coke formation, which was observed experimentally and numerically.

This study also reveals that the chemical models applied – even though the most detailed ones available were used – need further improvement. Potential extensions of the models are seen in the implementation of more sophisticated coking models and a more detailed description of adsorption of higher hydrocarbons (surface chemistry) and the evaluation of the gas-phase mechanism applied.

Furthermore, the numerical algorithms need to be strengthened as well to be able to include a heat balance in a two-dimensional simulation that includes thousands of reactions, because studies on CPOX of light hydrocarbons [40] revealed the strong impact of temperature on the interaction of catalytic and gas-phase chemistry.

The recently developed algorithms and implementation in the computer code DETCHEM^{CHANNEL} permits, for the first time, two-dimensional simulations of reactive flows in chemical reactors with catalytic and non-catalytic fuel conversion using reaction mechanisms that consist of over 800 chemical species. These models and computational tools, together with experimental studies in practical flow reactors at well-defined conditions, offer a new route for a better understanding of high-temperature catalysis and can support design and optimization of devices in energy-related catalysis.

Acknowledgments

Fruitful discussions with L.D. Schmidt (University of Minnesota), R.J. Kee (Colorado School of Mines), H.G. Bock, J. Schlöder, and late J. Warnatz (all Heidelberg University) were great help on setting-up the experiment and developing the computational

tools. We are thankful to C. Westbrook (Lawrence Livermore National Lab.) for sharing the gas-phase reaction mechanism. We thank the Umicore AG (Hanau/Germany) for providing the model catalyst for free. This study was financially supported by the German Research Foundation (DFG).

References

- [1] A. Lindermeir, S. Kah, S. Kavurucu, M. Muhlner, *Appl. Catal.*, A 70 (2007) 488–497.
- [2] B.J. Dreyer, I.C. Lee, J.J. Krummenacher, L.D. Schmidt, *Appl. Catal.*, A 307 (2006) 184–194.
- [3] A.D. Qi, S.D. Wang, C.J. Ni, D.Y. Wu, *Int. J. Hydrogen Energy* 32 (2007) 981–991.
- [4] R.P. O'Connor, E.J. Klein, L.D. Schmidt, *Catal. Lett.* 70 (2000) 99–107.
- [5] S. Jain, H.-Y. Chen, J. Schwank, *J. Power Sources* 160 (2006) 474–484.
- [6] L. Bobrova, I. Zolotarsky, V. Sadykov, V. Sobyanyan, *Int. J. Hydrogen Energy* 32 (2007) 3698–3704.
- [7] J. Thormann, L. Maier, P. Pfeifer, U. Kunz, K. Schubert, O. Deutschmann, *Int. J. Hydrogen Energy* 34 (2009) 5108–5120.
- [8] L.F. Brown, *Int. J. Hydrogen Energy* 26 (2001) 381–397.
- [9] C. Severin, S. Pischinger, J. Ogrzewalla, *J. Power Sources* 145 (2005) 675–682.
- [10] J. Lawrence, M. Boltze, *J. Power Sources* 154 (2006) 479–488.
- [11] G. Kolb, V. Cominos, C. Hofmann, H. Pennemann, J. Schurer, D. Tiemann, M. Wichert, R. Zapf, V. Hessel, H. Lowe, *Chem. Eng. Res. Des.* 83 (2005) 626–633.
- [12] O. Deutschmann, L.D. Schmidt, *AIChE J.* 44 (1998) 2465–2476.
- [13] R. Quiceno, J. Pérez-Ramírez, J. Warnatz, O. Deutschmann, *Appl. Catal.*, A 303 (2006) 166–176.
- [14] M. Geske, K. Pelzer, R. Horn, F.C. Jentoft, R. Schlögl, *Catal. Today* 142 (2009) 61–69.
- [15] D.K. Zerkle, M.D. Allendorf, M. Wolf, O. Deutschmann, *J. Catal.* 196 (2000) 18–39.
- [16] A. Beretta, E. Ranzi, P. Forzatti, *Chem. Eng. Sci.* 56 (2000) 779–787.
- [17] A. Beretta, L. Piovesan, P. Forzatti, *J. Catal.* 184 (1999) 455–468.
- [18] R. Schwiedernoch, S. Tischer, C. Correa, O. Deutschmann, *Chem. Eng. Sci.* 58 (2003) 633–642.
- [19] D. Dalle-Nogare, N.J. Degenstein, R. Horn, P. Canu, L.D. Schmidt, *Catal. Today* 258 (2008) 131–142.
- [20] M. Hartmann, S. Lichtenberg, N. Hebben, D. Zhang, O. Deutschmann, *Chem. Ing. Tech.* 81 (2009) 909–919.
- [21] M. Hartmann, T. Kaltschmitt, O. Deutschmann, *Catal. Today* 147 (2009) S204–S209.
- [22] H.D. Minh, H.G. Bock, S. Tischer, O. Deutschmann, in: O. Gervasi, B. Murgante (Eds.), *Lecture Notes in Computer Science*, vol. 507, Springer-Verlag, Heidelberg, 2008, pp. 1121–1130.
- [23] H.D. Minh, H.G. Bock, S. Tischer, O. Deutschmann, *AIChE J.* 54 (2008) 2432–2440.
- [24] O. Deutschmann, S. Tischer, S. Kleditzsch, V.M. Janardhanan, C. Correa, D. Chatterjee, N. Mladenov, H. D. Minh, DETCHEM™ Software Package, 2.2 ed., Karlsruhe, 2008. <<http://www.detchem.com>>.
- [25] R. Kee, M. Coltrin, P. Glarborg, *Chemically Reacting Flow*, first ed., Wiley-Interscience, Weinheim, 2003.
- [26] L. Raja, R. Kee, O. Deutschmann, J. Warnatz, L.D. Schmidt, *Catal. Today* 59 (2000) 47.
- [27] S. Tischer, C. Correa, O. Deutschmann, *Catal. Today* 69 (2001) 57–62.
- [28] O. Deutschmann, in: G. Ertl, H. Knözinger, F. Schüth, J. Weitkamp (Eds.), *Handbook of Heterogeneous Catalysis*, second ed., Wiley-VCH, Weinheim, 2008, pp. 1811–1828.
- [29] H.J. Curran, P. Gaffuri, W.J. Pitz, C. K Westbrook, *Combust. Flame* 129 (2002) 253–280.
- [30] O. Deutschmann, R. Schwiedernoch, L. Maier, D. Chatterjee, in: E. Iglesia, J.J. Spivey, T.H. Fleisch (Eds.), *Natural Gas Conversion, Studies in Surface Science and Catalysis*, vol. VI, Elsevier, New York, 2001, pp. 215–258.
- [31] A.T. Bell, in: E. Shustorovich (Ed.), *Chemisorption and Surface Diffusion*, Wiley-VCH, Weinheim, 1991 (Chapter 5).
- [32] E. Shustorovich, H. Sellers, *Surf. Sci. Rep.* 31 (1998) 1–119.
- [33] A.V. Zeigarnik, R.E. Valdes-Perez, O.N. Myatkovskaya, *J. Phys. Chem. B* 104 (2000) 10578–10587.
- [34] Y. Qiang, W. Tinghua, Y. Lefu, L. Chunrong, W. Weizheng, W. Zisheng, W. Huilin, *J. Nat. Gas Chem.* 9 (2000) 1–7.
- [35] N.J. Degenstein, R. Subramanian, L.D. Schmidt, *Appl. Catal.*, A 305 (2006) 146–159.
- [36] G.J. Panuccio, K.A. Williams, L.D. Schmidt, *Chem. Eng. Sci.* 61 (2006) 4207–4219.
- [37] M. Bizzi, R. Schwiedernoch, O. Deutschmann, G. Saracco, *AIChE J.* 50 (2004) 1289–1299.
- [38] R. Horn, K.A. Williams, N.J. Degenstein, A. Bitsch-Larsen, D.D. Nogare, S.A. Tupy, L.D. Schmidt, *J. Catal.* 249 (2007) 380–393.
- [39] A. Beretta, G. Groppi, M. Lualdi, I. Tavazzi, P. Forzatti, *Ind. Eng. Chem. Res.* 48 (2009) 3825–3836.
- [40] S. Karagiannidis, J. Mantzaras, R. Bombach, S. Schenker, K. Boulouchos, *Proc. Combust. Inst.* 32 (2009) 1947–1955.
- [41] C.V. Naik, A.M. Dean, *Proc. Combust. Inst.* 32 (2009) 437–443.
- [42] N. Mladenov, J. Koop, S. Tischer, O. Deutschmann, *Chem. Eng. Sci.* 65 (2010) 812–826.